On the nonlinear dynamics of self-sustained limit-cycle oscillations in a flapping-foil energy harvester

Enhao Wang [a], Kiran Ramesh [b,*], Shaun Killen [c], Ignazio Maria Viola [d]

[a] *State Key Laboratory of Hydraulic Engineering Simulation and Safety, Tianjin University, Tianjin 300072, China*

[b] *Aerospace Sciences Division, School of Engineering, University of Glasgow, Glasgow, G12 8QQ, UK*

[c] *Institute of Biodiversity, Animal Health, and Comparative Medicine, University of Glasgow, Glasgow, G12 8QQ, UK*

[d] *School of Engineering, Institute for Energy Systems, University of Edinburgh, Edinburgh, EH9 3DW, UK*

ARTICLE INFO

ABSTRACT

The nonlinear dynamics of an airfoil at Reynolds number $Re = 10,000$ constrained by two springs and subject to a uniform oncoming flow is studied numerically. The studies are carried out using open source computational fluid dynamics toolbox OpenFOAM. Under certain conditions related to aerodynamic flutter, this two-degree-of-freedom system undergoes self-sustained limit-cycle oscillations (LCOs) with potential application as an energy harvester. When the system is given a small initial perturbation, it is seen that the response of the system decays to zero at flow velocities below the flutter velocity, or oscillates in a limit cycle at velocities greater than the flutter velocity. The flutter velocity at $Re = 10,000$ is shown to deviate significantly from the theoretical prediction (which is derived with an assumption of infinite Reynolds number) owing to the effect of viscosity. The LCOs at freestream velocities higher than the flutter velocity result in unsteady flows that are heavily influenced by leading-edge vortex shedding as well as trailing-edge flow separation. The influence of different system parameters on the onset of flutter and on the limit-cycle response characteristics is investigated in this research. This is done by defining a baseline case and examining the effects of varying aerodynamic parameters such as freestream velocity, and structural parameters such as the pitch-to-plunge frequency ratio and the type of spring stiffnesses. The conditions corresponding to the lowest flutter velocities (and consequently the lowest "cut-in" speeds for power extraction) and the parameter space that provide single-period, single-amplitude and harmonic LCOs (ideal for power extraction) are identified. Calculation of instantaneous and time-averaged power is presented by modeling the extraction of energy through a viscous damper. The highest power coefficients and efficiencies are obtained at velocities just higher than the flutter velocity. Introduction of positive cubic stiffening in the system springs is seen to make the system more stable, LCOs more harmonic and single-period, and to potentially increase power extraction efficiency of the system.

---

* Corresponding author.
   E-mail addresses: enhao.wang@tju.edu.cn (E. Wang), kiran.ramesh@glasgow.ac.uk (K. Ramesh), shaun.killen@glasgow.ac.uk (S. Killen), i.m.viola@ed.ac.uk (I.M. Viola).

Nomenclature

α	Pitch angle
α_A, h_A	Amplitude of LCO in pitch and plunge
$\bar{\omega} = \omega_h/\omega_\alpha$	Frequency ratio
β_α, β_h	Coefficient of cubic stiffening in pitch and plunge
$\dot{\alpha}^* = d\alpha/dt^*$	Nondimensional pitch rate
$\dot{h}^* = d(h/c)/dt^*$	Nondimensional normalized plunge rate
η_P	Power capture efficiency
$\kappa = \pi\rho c^2/4m$	Inverse mass ratio
$\omega = 2\pi/T$	Angular frequency of sinusoidal motion
$\omega_\alpha = \sqrt{k_\alpha/I_\alpha}$	Characteristic frequency of pitch mode
$\omega_h = \sqrt{k_h/m}$	Characteristic frequency of plunge mode
$\overline{C_P}$	Time-averaged power coefficient
$\zeta_h = c_h/2m\omega_h$	Nondimensional damping ratio for plunge
c	Airfoil chord
C_l, C_d, C_m	Lift coefficient, drag coefficient and pitching-moment coefficient, per unit span
C_P	Power coefficient per unit span
C_W	Nondimensional accumulated work per unit span
c_α, c_h	Pitch and plunge structural damping coefficient, per unit span
$F(\alpha), F(h)$	Restoring force by rotational (pitch) and translational (plunge) springs
h	Plunge displacement
I_α	Airfoil moment of inertia about pivot
$k = \omega c/2U$	Reduced frequency of sinusoidal motion
k_α, k_h	Linear pitch and plunge stiffness, per unit span
m	Mass of airfoil
$r_\alpha = 2\sqrt{I_\alpha/mc^2}$	Airfoil radius of gyration about pivot
Re	Reynolds number based on c and U
S_α	Static moment of airfoil about pivot
T	Time period of sinusoidal motion
t	Physical time
$t^* = tU/c$	Non-dimensional time
U	Freestream velocity
$U^* = U/\omega_\alpha c$	Nondimensional velocity
U_F	Flutter velocity
$x_\alpha = 2S_\alpha/mc$	Distance of center of gravity aft of pivot, nondimensionalized by c
DOF	Degree of freedom
LCO	Limit-cycle oscillation
LEV	Leading-edge vortex
TEV	Trailing-edge vortex

1. Introduction

Classical aeroelasticity treats fluid–structure interaction and its associated phenomena (such as divergence, control reversal and flutter) as undesirable (Bisplinghoff and Ashley, 1996; Fung, 2002), but recent studies have shown that it to beneficial in biological flight and swimming (Hamamoto et al., 2007; Nakata and Liu, 2012; Taylor et al., 2010). One potential application is the development of novel energy harvesters mimicking the motion of fish tails and based on the principle of aerodynamic flutter, using the motion of a flapping wing to drive a generator (Young et al., 2014). These harvesters claim significant advantages over the majority of existing wind/water energy harvester designs which utilize horizontal-axis or vertical-axis turbines and present challenges related to economic viability and environmental impact (Xiao and Zhu, 2014).

The objective of this research is to investigate the nonlinear aeroelasticity and dynamics of the flapping-foil energy harvester in the $Re = 10,000$ regime through a detailed parametric study. The system consists of a two-degree-of-freedom (2DOF) foil constrained by rotational and translational springs. The system may exhibit various responses at different freestream velocities, depending on the several aerodynamics and structural parameters that govern the system. The ideal response for power generation is expected to be single-period, single-amplitude oscillations, and hence it is important to characterize the response and behavior of the system as a function of the various underlying parameters.

The flapping-wing harvester offers promise of power generation at lower flow velocities, with no centrifugal stress associated with rotating blades, and with lesser noise generation and impact on the environment owing to lower tip speeds (Young et al., 2014; Xiao and Zhu, 2014; Shimizu et al., 2008). Unlike conventional aerodynamic wings and rotary turbines which require smooth attached flow for maximum efficiency, these energy harvesters mimic fish swimming in nature by promoting the formation of large vortical structures. In particular, a leading-edge vortex is periodically formed and shed to achieve high instantaneous forces (Ellington et al., 1996; Shyy and Liu, 2007; Ellington, 1999; Dickinson and Gotz, 1993) and high propulsive (Anderson et al., 1998) and power-extraction (Kinsey and Dumas, 2008) efficiencies. The sustained oscillation of the flapping wing results from fluid dynamic flutter, at freestream velocities at and above the linear flutter velocity.

Early works on theory of flutter based on linear aerodynamic formulations by Theodorsen (1935) and Theodorsen and Garrick (1942) can be used to predict the flutter velocity for a 2DOF airfoil at the inviscid limit of infinite Reynolds number. This is the freestream velocity at which the system becomes unstable and the airfoil oscillations start to grow exponentially. The presence of nonlinearities in the system, however, affects both the flutter velocity and the characteristics of the system response. These nonlinearities could be aerodynamic or structural in origin and often result in single-amplitude limit-cycle oscillations (LCOs), which can be used to extract power as described previously.

Structural nonlinearities may arise owing to large deformations, material properties, or loose linkages (Lee et al., 1999b). The effects of structural nonlinearities on airfoil aeroelasticity have been studied extensively, focusing on various types of nonlinear spring behavior such as bilinear or cubic variation in stiffness (see Refs. Lee et al., 1999a; Price et al., 1995). A comprehensive review of such studies is given by Lee et al. (1999b). These studies assume linear aerodynamics, that is, the flow is incompressible, inviscid and attached to the airfoil. These studies showed, for example, that hard springs (positive cubic stiffening) result in a supercritical Hopf bifurcation, where LCOs occur only at freestream velocities greater than the linear (theoretical/inviscid) flutter velocity and are independent of initial conditions. Soft springs (negative cubic stiffening), on the other hand, result in a subcritical Hopf bifurcation where LCOs may arise at velocities below the linear flutter velocity, depending on initial conditions. Further, chaotic oscillations were observed in a range of freestream velocities for some choices of parameters.

Aerodynamic nonlinearities may result from compressibility or viscous effects (Lee et al., 1999b). Limit-cycle oscillations resulting from nonlinear aerodynamics due to compressibility effects (transonic flows) have been studied by Bendiksen (2011). Nonlinear aerodynamics caused by viscous flow phenomena are largely dependent on the Reynolds number and the reduced frequencies involved, and leading-edge vortices (LEVs) have been seen to play a crucial role. In helicopter and wind-turbine applications, which are necessarily associated with large Reynolds numbers and low reduced frequencies, LEVs and the resulting dynamic stall phenomenon might lead to violent vibrations and mechanical failure (Leishman, 2002). On the other hand, LEVs in low Reynolds number, high-frequency flows have been credited with contributing toward the success of high-lift flight in insects (Ellington et al., 1996; Shyy and Liu, 2007; Ellington, 1999; Dickinson and Gotz, 1993), and high propulsive (Anderson et al., 1998) and power-extraction (Kinsey and Dumas, 2008; Jones et al., 2003) efficiencies. Amandolese et al. (2013) have shown experimentally that viscosity has a significant effect on the flutter velocity as well as the post-flutter system response.

In recent years, high-fidelity computational aerodynamics and structural solvers (CFD and CSD methods) coupled together have also been used to study nonlinear aeroelasticity accurately (for instance, Kamakoti and Shyy, 2004). Peng and Zhu (2009), Zhu et al. (2009), Young et al. (2013) and Zhu and Peng (2009) have used Navier–Stokes solvers coupled with structural models to study energy harvesting through flow-induced oscillations of a fully passive foil. Though time-consuming and expensive, such studies provide great insight into the underlying physics and nonlinear dynamics. The authors of all these studies report that LEV formation and shedding plays a key role in maximizing power-extraction efficiency of the system. Kinsey and Dumas (2008) have studied the power extraction efficiencies for various prescribed kinematics of the flapping foil and also arrived at the same conclusion relating to leading-edge vortex shedding and efficiency. Zhu and Peng (2009) have elucidated the vorticity control mechanism that results in this increased efficiency. A more recent numerical study by Wang et al. (2017) suggests that the high-efficiency scenario in a fully passive flapping-foil system is also associated with a large pitch–plunge phase and a "2S" wake pattern composed of two strong single leading-edge vortices shed per cycle.

Boundary element methods such as panel methods are based on distributions of singularities on the lifting surface and are well established in the literature for computing flapping-wing propulsion and power extraction (Jones et al., 0000, 2003). A subset of these are discrete-vortex methods which have been recently employed by several authors to simulate vortex-dominated unsteady flows such in several problems (Ramesh et al., 2013, 2014; Hammer et al., 2014; Xia and Mohseni, 2013; Wang and Eldredge, 2012; Liu et al., 2016). Ramesh et al. (2015) coupled such a discrete-vortex method that models LEV formation and shedding with a structural model to investigate the effect of aerodynamic and structural nonlinearities on the response of a fully-passive 2DOF flat plate. Their research showed that nonlinearity in the aerodynamics resulting from leading-edge vortex shedding is sufficient to cause limit-cycle behavior. At velocities just over the linear flutter velocity, single-period LCOs were seen, while at higher velocities, multi-period LCOs (of mixed frequencies and amplitudes) and subsequently divergent behavior were seen. It was also shown that the addition of positive cubic stiffening to the system, a structural nonlinearity, resulted in a larger velocity range of single-period LCOs (albeit of smaller amplitudes) and increased the velocity at which divergent behavior occurs. This study however did not model the other nonlinearities present in the aerodynamics such as the flow separation from the trailing edge of the airfoil and the effect of viscosity. Other low-order
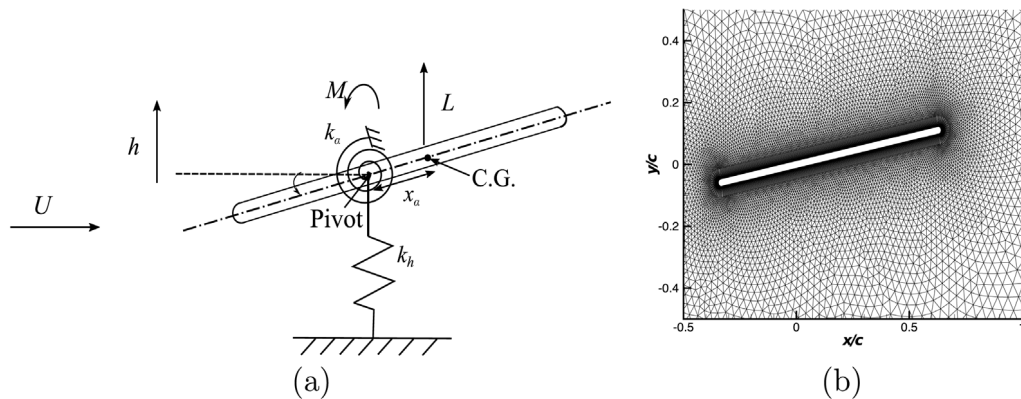
Fig. 1. (a) sketch of the physical configuration, and (b) close-up of computational mesh around the foil.

models that have been used to study this problem include semi-empirical ones such as the ONERA model used in Bryant et al. (2013) and Sarkar and Bijl (2008).

The flapping-wing energy harvester was first proposed by McKinney and DeLaurier (1981) and has since been the subject of numerous investigations aiming to optimize its design and performance as described earlier in this section. The growing importance of renewable energy harvesting, and the increased interest in unsteady aerodynamics inspired by flapping-wing MAVs and flexible lifting surfaces, has provided further impetus to this research area. Several implementations of this technology with varying levels of success and efficiency are reviewed in Young et al. (2014) and Xiao and Zhu (2014). Notably, Boragno et al. (2012) and Boccalero et al. (2017) have developed an efficient realization of the energy harvester through electromagnetic coupling in the Reynolds number range between 5000–10,000 for micro-power harvesting. They have also developed a simple low-order model of the system for analytical investigations, though this does not account for the nonlinear aerodynamics. In this paper, we do not aim to comment on the optimal design for this problem. Rather, we are interested in characterizing the dynamical responses of the setup in terms of the various underlying system parameters. With this aim, a high fidelity CFD solver is coupled with a 2DOF structural model to study the fluid–structure interaction phenomena and limit-cycle oscillations of a flat plate at $Re = 10,000$. The unsteady aerodynamics and associated nonlinearities in this Reynolds number regime are fairly well understood since they have been the subject of extensive investigation (Ramesh et al., 2013, 2014; Xia and Mohseni, 2013; Hammer et al., 2014; Wang and Eldredge, 2012; McGowan et al., 2011; Ol et al., 2009, 2010) in the last decade (inspired by MAV design). This Reynolds number also falls in an ideal regime where the shed leading-edge vortices are coherent (Boccalero et al., 2017). The effect of various aerodynamic and structural parameters on the 2DOF system's passive response characteristics (such as amplitude and frequency) and power generation potential are investigated in detail. These studies, in turn, are used to identify the ideal regimes of operation for the 2DOF flapping-foil harvester. The data generated through this research on limit-cycle characteristics as a function of various underlying parameters may be used in development and calibration of low-order models to simulate nonlinear airfoil aeroelasticity (such as those based on discrete vortices and semi-empirical fitting, discussed previously).

The outline for the rest of the paper is as follows. A detailed description of the theory and numerical methods employed in this research along with suitable validation are provided in Section 2. The parametric study is carried out in Section 3 and the dependence of LCO characteristics on the relevant structural and aerodynamics parameters is presented and studied. Finally, the conclusions drawn from this study are listed in Section 4 and the paper summarized.

2. Numerical methods for aeroelastic modeling

An unsteady aeroelastic solver for a fully passive 2DOF airfoil is presented in this section. For the aerodynamics, high-fidelity 2D unsteady computations are performed at Reynolds number of 10,000 using the open-source CFD toolbox OpenFOAM. The structural dynamic solver adopted in the present study is able to account for geometric nonlinearities in the kinematics and for nonlinear spring stiffnesses.

The aeroelastic system subject to study is shown in Fig. 1(a). A rigid flat plate is elastically supported in plunge, h, and pitch, α, and is subject to a uniform freestream velocity U. The corresponding generalized forces for the pitch and plunge coordinates are lift, L, and pitching moment, M, respectively. The structural parameters of the system — linear spring stiffnesses k_h and k_α, and static unbalance x_α are also depicted in Fig. 1(a). The pivot refers to the chordwise location on the airfoil at which the springs are attached (often referred to as elastic axis or pitch axis in aeroelasticity literature).

2.1. Flow model

The fluid flow around the flat plate is modeled by solving the unsteady incompressible Navier–Stokes equations in conjunction with the Spalart–Allmaras (SA) turbulence model (Spalart and Allmaras, 1992). The SA model is chosen for this

problem because of extensive experience in applying it successfully for unsteady, separated and vortex-dominated flows at $Re = 10{,}000$ such as those considered in this research (McGowan et al., 2011; Ramesh et al., 2013, 2014). Research has also shown that this problem is not very sensitive to choice of turbulence modeling. For example, Ol et al. (2009) have used the $k - \omega$ model and reported no significant differences in the flow evolution and force histories. Visbal (2009) has studied a plunging airfoil, again at $Re = 10{,}000$, with high-fidelity large eddy simulations and concluded that transitional effects are minimal. Even at a higher Reynolds numbers of 60,000 where the effects of turbulence model selection are expected to be more important, Catalano and Tognaccini (2010) have shown in a comparative study of various turbulence models, that the SA achieves good results including prediction of laminar separation bubbles. In the present study at low Re (10,000), the trip terms f_{t1} and f_{t2} in the originally published version are turned off and at the same time the "trip-less" initial condition for $\widetilde{\nu}$ is used following Travin et al. (2000).

The governing equations are solved using the open source CFD toolbox OpenFOAM based on a finite volume method (FVM). A second-order backward implicit scheme is adopted to discretize the transient terms, while second-order Gaussian integration schemes with linear interpolation for the face-centered values of the variables are used for the gradient, divergence and Laplacian terms. The pressure implicit with splitting of operators (PISO) algorithm is employed to achieve pressure–velocity coupling.

A close-up of the computational mesh (from a grid study presented later) is shown in Fig. 1(b). There are 560 nodes along the circumference of the flat plate and the minimum mesh size next to the flat plate surface in the radial direction is $0.001c$, where c is the chord length of the flat plate. The nondimensional mesh size next to the flat plate surface is found to be $y^+ < 1$, where y^+ is defined as $y^+ = u_f y / \nu$ with u_f being the friction velocity and y being the distance to the nearest wall. The boundary conditions for the governing equations are as follows. The surface of the flat plate is assumed to be smooth, where no-slip boundary condition is employed. The inflow velocity and turbulence properties are set to be the same as the freestream values. At the outflow boundary, the gradients of the flow velocity in the streamwise direction is set to zero and the same turbulence properties as the freestream ones are considered. On the two transverse boundaries, the velocity in the direction normal to the boundary is zero and the freestream turbulence properties are adopted.

2.2. Structural model

The kinetic energy T and potential energy U of the aeroelastic system shown in Fig. 1(a) are given by

$$
\begin{aligned}
T &= \frac{1}{2}m\dot{h}^2 - S_\alpha \cos\alpha \, \dot{h}\dot{\alpha} + \frac{1}{2}I_\alpha \dot{\alpha}^2 \\
U &= \int_0^h F_h \, dh + \int_0^\alpha F_\alpha \, d\alpha
\end{aligned}
\tag{1}
$$

Applying Lagrange's equations to the system with pitch (α) and plunge (h) as the generalized coordinates, the dynamical model is derived as

$$
\begin{aligned}
m\ddot{h} - S_\alpha \ddot{\alpha}\cos\alpha + S_\alpha \dot{\alpha}^2 \sin\alpha + c_h \dot{h} + F_h &= L, \\
-S_\alpha \cos\alpha \, \ddot{h} + I_\alpha \ddot{\alpha} + c_\alpha \dot{\alpha} + F_\alpha &= M,
\end{aligned}
\tag{2}
$$

where ($\bullet$) indicates differentiation with respect to time, m is the total mass of the airfoil, and S_α and I_α are its static and inertia moments about the pivot; c_h and c_α are structural damping coefficients for plunge and pitch coordinates; $F_h = F_h(h)$ and $F_\alpha = F_\alpha(\alpha)$ are the restoring forces in plunge and pitch, respectively, and can include any spring nonlinearity such as cubic hardening/softening, bilinearity or hysteresis (Lee et al., 1999b). The interested reader may refer to Ramesh et al. (2015) for more details and the complete derivation. In the present research, only cubic stiffening nonlinearity is considered, for which

$$
\begin{aligned}
F_h(h) &= k_h(h + \beta_h h^3) \\
F_\alpha(\alpha) &= k_\alpha(\alpha + \beta_\alpha \alpha^3)
\end{aligned}
\tag{3}
$$

Eq. (2) is solved using a Newmark integration method (Newmark, 1959) with second-order accuracy, and with initial conditions representing a small disturbance, $\alpha(0) = 10°$ and $\dot{\alpha}(0) = h(0) = \dot{h}(0) = 0$.

2.3. Fluid–structure interaction

The fluid–structure interaction is based on a loosely coupled approach with a correspondingly small time step. In this approach, information is exchanged at each time step but no subiterations are performed. The fluid–structure interaction procedure within one simulation time step is briefly summarized below:

1. The flow equations are solved to obtain the aerodynamic loads on the flat plate.
2. These aerodynamic loads are applied to the structural solver to yield the motion quantities of the flat plate.
3. Spherical linear interpolation (SLERP) of the motion quantities as a function of distance to the objective surfaces is performed to update the computational mesh.
4. The next time step begins with solving the flow equations on the updated mesh.

Table 1
LCO results for the baseline parameter set from uniformly refined grids.

Mesh	$N_{element}$	N_c	$\Delta r/c$	α_A (deg)	h_A/c	$k(\alpha)$	$k(h)$	ϕ (deg)
1 (base)	24 488	560	0.0050	68.11	0.2254	0.3464	0.3464	29.44
2	48 590	1120	0.0010	69.50	0.2314	0.3453	0.3453	29.82
3	99 576	2240	0.0005	69.97	0.2307	0.3471	0.3471	29.91

2.4. Available power and capture efficiency

Extraction of power from the dynamical system through a generator is typically modeled using a viscous damper (Zhu and Peng, 2009; Zhu et al., 2009). Considering a setup where energy is extracted from the plunge degree of freedom, the instantaneous power is given by,

$$P = c_h \dot{h}^2 \tag{4}$$

Using the definitions presented in this paper, the power coefficient is calculated in terms of nondimensional parameters as,

$$C_P = \frac{P}{\frac{1}{2}\rho U^3 c} = \pi \frac{\zeta_h (\dot{h}^*)^2}{\kappa} \frac{\omega_h c}{U} \tag{5}$$

where ζ_h is the nondimensional damping ratio in plunge. The time-averaged power ($\overline{P}$) and power-coefficient ($\overline{C_P}$) are obtained by averaging the instantaneous values over an oscillation cycle (after stable LCOs are reached).

Estimating the total energy available in the flow in terms of the area swept by the oscillating airfoil (Dunnmon et al., 2011), the capture efficiency η_P may be approximated as

$$\eta_P = \frac{\overline{C_P}}{(h/c)_{max} - (h/c)_{min}} \tag{6}$$

2.5. Verification

The numerical uncertainty for the simulations performed in this research is quantified using the method proposed by Viola et al. (2013). The baseline parameter set of aerodynamic and structural system parameters introduced in Section 3.1 are used here. Simulations of the aeroelastic system with meshes of increasing resolutions are performed, and the uncertainty quantified for the LCO characteristics α_A, h_A, $k(\alpha)$ and ϕ. Here, α_A and h_A are the amplitudes of pitch and plunge limit-cycle responses, $k(\alpha)$ is the reduced frequency of pitch response, and ϕ is the phase by which pitch leads plunge.

This method was initially developed for yacht sail aerodynamics but it can be applied to any other application. The method is as follows: the 95% confidence interval of any computed value is given by twice the product of the normalized numerical uncertainty U_{num} and the computed value. For example, for the angle of attack, $\alpha \pm U_{num}\alpha$.

Here we assume that the numerical uncertainty is governed by the grid uncertainty, i.e. that the uncertainties due to other sources of errors such as, for instance, the time step and the iterative convergence are negligible. To compute U_{num}, simulations with three different grid sizes are performed. The number of elements $N_{element}$ of the three grids is shown in the second column of Table 1. The base grid, for which the uncertainty is computed, is the coarsest grid (Mesh 1). The two finest grids were achieved by a uniform refinement.

The relative step size h_i is defined as the ratio of the cell sizes of the ith grid to that of the base grid; and Φ_i as the ratio of the quantity for which the uncertainty is assessed computed with the ith grid to that computed with the base grid. For example, for the angle of attack, Φ_2 is the ratio between α computed with Mesh 2 and α computed with Mesh 1.

As h approaches zero, the fit of Φ_i should converge to Φ_0 with the order p of the adopted numerical scheme (see for instance, Fig. 2). Given that different schemes are used to solve the coupled system of equations, p is generally unknown. Therefore, a curve

$$\Phi(h) = \Phi_0 + ah^p \tag{7}$$

is fitted through the computed Φ_i. The parameters $\{\Phi_0, \alpha, p\}$ can be estimated by a least squares method for any number of tested grids.

If the fitted curve converges asymptotically towards Φ_0 (here we state this condition as $p \geq 0.95$), then the extrapolated value Φ_0 is the expected value of Φ for an infinitely fine grid. This allows estimating the error of the base grid as

$$\delta = |1 - \Phi_0|. \tag{8}$$

The grid uncertainty is then given by

$$U_{num} = 1.25\delta \tag{9}$$
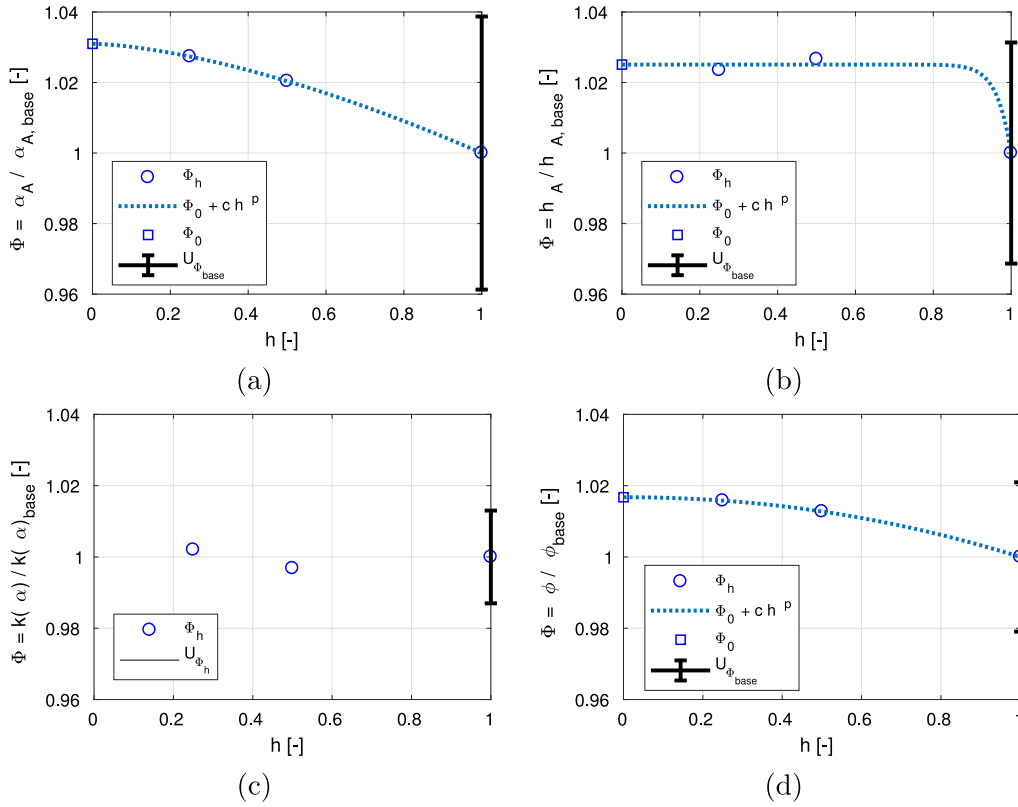
where 1.25 is a safety factor (Roache, 1998).

Fig. 2. Uncertainty quantification for (a) α_A, (b) h_A, (c) $k(\alpha)$ and (d) ϕ, where Φ is the ratio between the value computed with different grids with that computed with the base grid (Mesh 2), and h is the ratio of the cell sizes to that of the base grid. The error bars show the normalized uncertainty U_{num}.

If the fitted curve does not converge ($p < 0.95$), then we estimate the error of the base grid as

$$\delta = \max(\Phi_{h_i}) - \min(\Phi_{h_i}), \tag{10}$$

and the grid uncertainty is computed as

$$U_{num} = 1.5\delta, \tag{11}$$

where 1.5 is a more cautious safety factor (Roache, 1998).

The computed values of α, h_a, $k(\alpha)$ and ϕ for the three grids are presented in Table 1. The fit with Eq. (7) of the computed values of α, h_a and ϕ, resulted in converging trends with $p \geq 0.95$, hence the uncertainty was computed with Eq. (9). Conversely, convergence was not found for $k(\alpha)$ and, hence, the uncertainty was computed with Eq. (11). The maximum uncertainty, however, is smaller than 4% for each of these values. In particular, we found,

$$\alpha = \alpha \pm 0.039\alpha; \qquad\qquad h_A = h_A \pm 0.031h_A;$$
$$k(\alpha) = k(\alpha) \pm 0.013k(\alpha); \qquad\qquad \phi = \phi \pm 0.021\phi.$$

2.6. Validation

The numerical methods discussed above are validation against published experimental and numerical data in this section. As published data for fully passive fluid–structure interaction at low Reynolds number is virtually non-existent, validation is presented for prescribed kinematics.

Data from Ramesh et al. (2013) for the ramp–hold–return pitch kinematics given by Eldredge's canonical formulation (Ol et al., 2010) is used to validate the flow model used in this paper. The reader may refer to Ramesh et al. (2013) for detailed information about the kinematic equations and the experimental and computational methods used. This dataset is chosen for validation because of being at the same $Re = 10,000$, similar flat plate geometry, and similar flow physics involving massive flow separation and vortex shedding.

Pitch ramp motions with amplitudes of $25°$ and $45°$, and pivot about leading edge are considered. The pitch history for these motions is shown on the right axis in Fig. 3. On the left axis, lift and drag coefficients from the current CFD method are compared against predictions from experiment and CFD published in Ramesh et al. (2013).
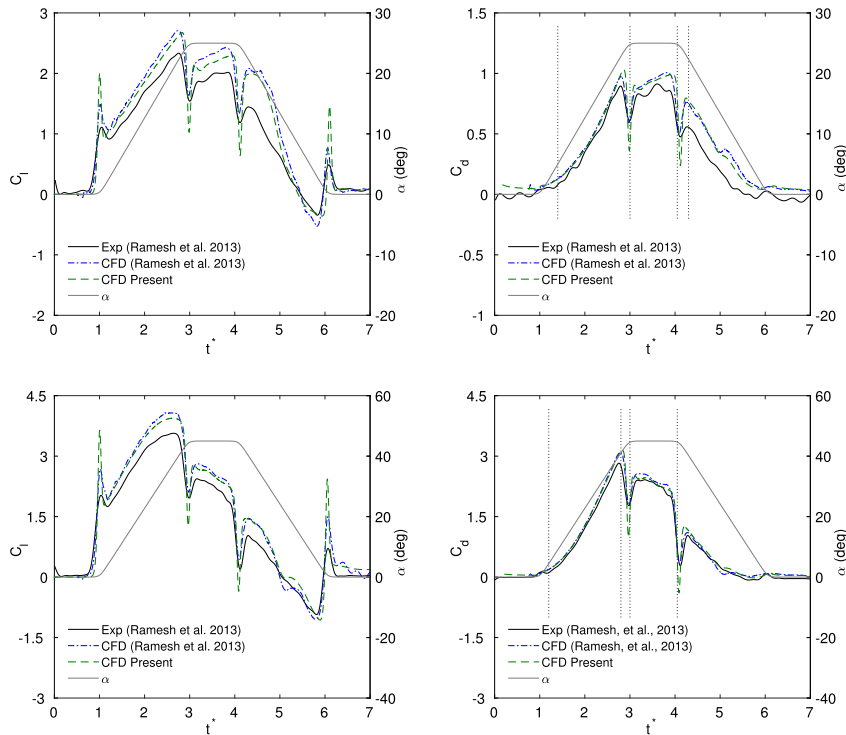
Fig. 3. 25° (top) and 45° (bottom) ramp–hold–return pitch about leading edge: comparison of lift coefficient (left) and drag coefficient (right) from present CFD method against experimental and CFD data published by Ramesh et al. (2013). Dotted vertical lines depict the time instants used to visualize flow in Fig. 4.

Fig. 3 shows that the force predictions from the current method compare very well with published data, with the acceleration peaks at the ramp corners being better resolved in the current method. In Fig. 4, experimental dye flow-visualization plots for these cases from Ramesh et al. (2013) are compared against vorticity contours from the current CFD method. The time instants at which flow is compared are marked in Fig. 3 and have been selected to depict various stages of LEV evolution in the two cases.

Comparison of the flow fields shows that the shapes and locations of the separated shear layers and vortex structures, and their convection, are predicted correctly by the current CFD model. This establishes confidence in using this model for studying fully passive fluid–structure interaction in the next section.

3. Results and discussion

In this section, the flutter velocity and LCO characteristics of the aeroelastic system described in Section 2 are investigated. In Section 3.1, a baseline set of structural and aerodynamic parameters are defined, and LCO response characteristics for this case are presented. In Section 3.2, the effect of increasing freestream velocity on the system response is investigated. The natural frequencies of the pitch and plunge modes depend on the spring stiffnesses, and mass and inertia of the plate (as defined in the nomenclature). The ratio of plunge natural frequency to pitch natural frequency gives the frequency ratio $\overline{\omega}$. This parameter, an important structural property of the system, is systematically varied in Section 3.3 and its influence on onset of flutter and LCOs is studied. Variation in spring stiffness through the addition of positive cubic stiffening is investigated in Section 3.4. The effect of initial conditions and subcritical oscillations of the aeroelastic system are studied in Section 3.5. Finally, power extraction from the system (modeled through viscous damping) is studied in Section 3.6.

3.1. Baseline case

The base parameter set for the numerical simulations performed in this study is listed in Table 2. A 2.3%-thick flat plate with semi-circular leading and trailing edges is considered. The chord length is chosen as a reference length scale and typical representative values for the structural parameters are chosen. The nondimensional distance of the pivot aft of the leading edge is $x_p = 0.35$, the static unbalance of the flat plate is $x_\alpha = 0.05$, its radius of gyration $r_\alpha = 0.5$, frequency ratio $\overline{\omega} = 0.25$, and inverse mass ratio $\kappa = 0.05$. No cubic stiffening is added (the springs are linear), no structural damping is included, and the initial condition is a 10° pitch displacement.
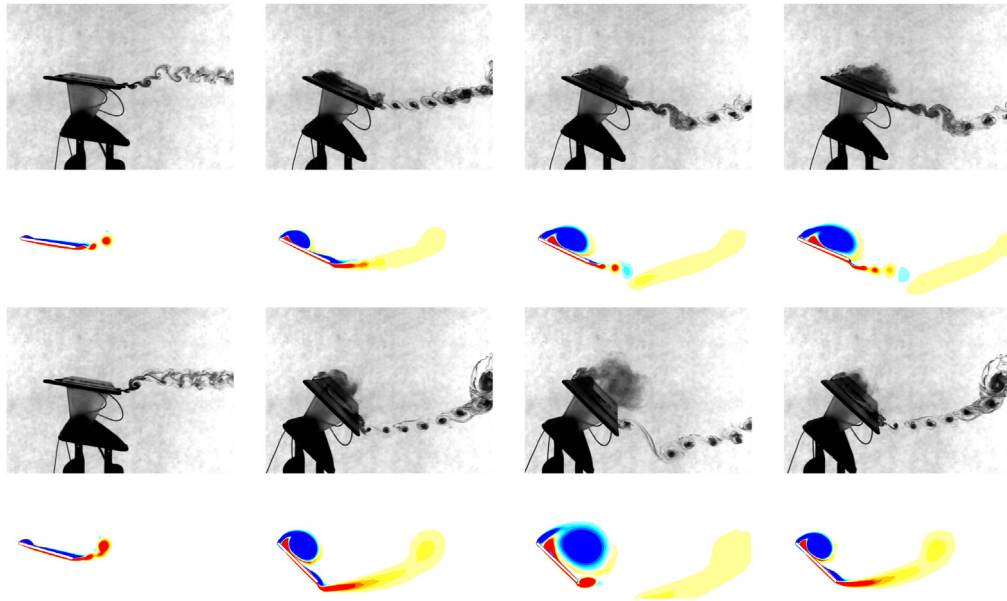
Fig. 4. 25° (top two rows) and 45° (bottom two rows) ramp–hold–return about leading edge: flow visualization comparison between experiments from Ramesh et al. (2013) and present CFD at four instants during the motion. The corresponding time instants are marked in Fig. 3.

Table 2
Base parameter set used in the present study.

Parameter	Symbol	Value
Pivot location (0–1)	x_p	0.35
Static unbalance	$x_\alpha = 2S_\alpha/mc$	0.05
Radius of gyration	$r_\alpha = 2\sqrt{I_\alpha/mc^2}$	0.5
Inverse mass ratio	$\kappa = \pi\rho c^2/4m$	0.05
Frequency ratio	$\overline{\omega} = \omega_h/\omega_\alpha$	0.25
Cubic stiffening − pitch	β_α	0.0
Cubic stiffening − plunge	β_h	0.0
Damping ratios	ζ_h, ζ_α	0.0, 0.0
Flutter velocity	U_F^*	1.55
Freestream velocity	U^*	1.6 ($U^*/U_F^* = 1.03$)
Initial conditions − pitch	$\alpha(0), \dot{\alpha}(0)$	$\alpha(0) = 10°, \dot{\alpha}(0) = 0$
Initial conditions − plunge	$h(0), \dot{h}(0)$	$h(0) = \dot{h}(0) = 0$

The flutter velocity for the baseline configuration is found to be $U_F^* = 1.55$. At all values of freestream velocity below the flutter velocity, the system has positive damping and its response decays from the provided initial condition to zero. At the flutter velocity, the system has zero damping and undergoes oscillations based on the initial disturbance with no growth or decay. At higher velocities, the system is negatively damped. According to linear aeroelastic theory, the pitch and plunge oscillations of the system should increase indefinitely. However, when the pitch and plunge oscillations are sufficiently large, flow separation and vortex shedding occur. These aerodynamic nonlinearities prevent the response from increasing indefinitely, resulting in limit-cycle oscillations (Ramesh et al., 2015). The LCOs of the baseline system at a freestream velocity just above the flutter velocity, $U^* = 1.03U_F^*$ are presented in Fig. 5.

Fig. 5(a) and (b) show the limit-cycle responses in pitch and plunge against nondimensional time after a "steady-state" is reached. The insets in these plots show the entire history of the response, increasing from the given initial condition to the limit-cycle state. Fig. 5(c), (d) and (e) are plots of the lift, drag and pitching moment coefficients for the flat plate, which also exhibit LCOs. Figs. (f) and (g) are phase-plane diagrams of the pitch and plunge responses, and (h) and (i) are plots of their Power Spectral Density (PSD) depicting the frequency of response. It is evident from the last four subplots that the responses are single-amplitude and single-period. The horizontal axis on the PSD plots is the reduced frequency k. The reduced frequencies of the pitch and plunge responses are seen to have the same value.

Fig. 6 shows the vorticity contours during one period of LCO for the baseline case, at four equally spaced instants in the cycle. It is seen that leading-edge vortices are shed alternatively from the upper and lower surfaces of the flat plate: (a) and (b) show an LEV forming on and being shed from the lower surface of the flat plate, (c) and (d) show an LEV forming on and being shed into the wake from the flat plate upper surface. Fig. 6(e) shows the trailing wake structure ensuing from LCOs and shed vortices.
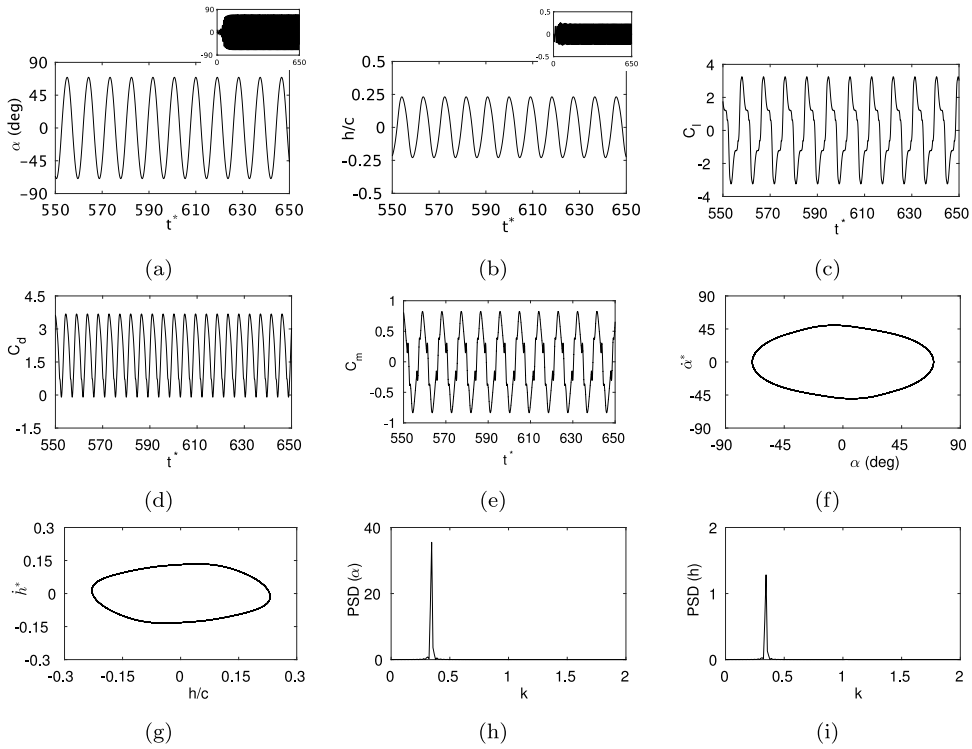
Fig. 5. Baseline case: limit-cycle response for the parameters listed in Table 2. Time variation of (a) pitch angle, (b) plunge per unit chord, (c) lift coefficient, (d) drag coefficient and (e) pitching moment coefficient. Plots (f) and (g) are phase-plane plots for pitch and plunge responses, (h) and (i) are PSD plots (in dB/Hz) for the pitch and plunge responses.
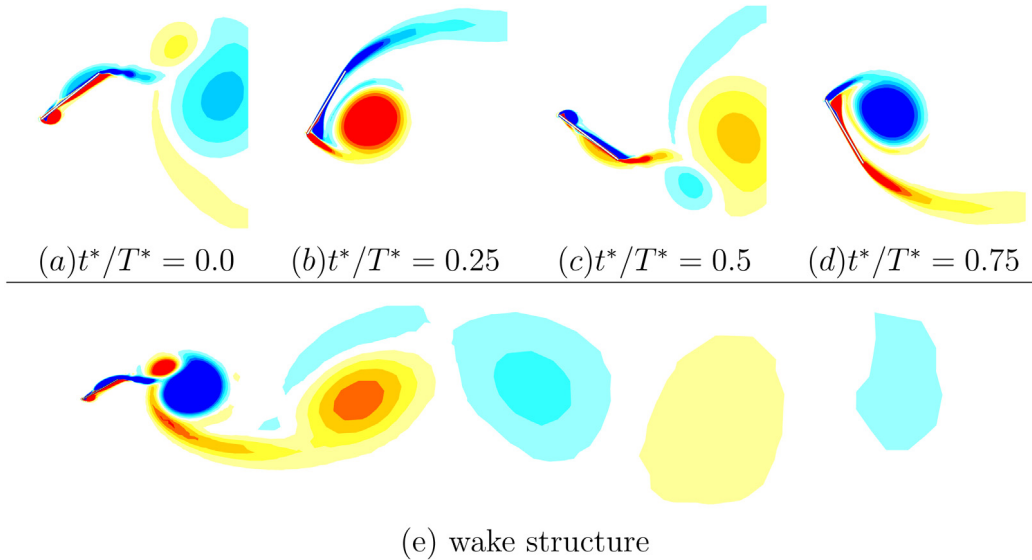

Fig. 6. Baseline case: vorticity contours for the limit-cycle response at four equally spaced time intervals over one period of oscillation (top), wake structure (bottom).

3.2. Effect of freestream velocity

In this section, the effect of increasing freestream velocity on the aeroelastic response of the system is studied. In addition to the baseline freestream velocity which is just over the flutter velocity ($1.03 U_F^*$), two higher velocities ($5 U_F^*$ and $10 U_F^*$) are considered. All other parameters are maintained at their baseline values. Comparison of the LCO characteristics for these
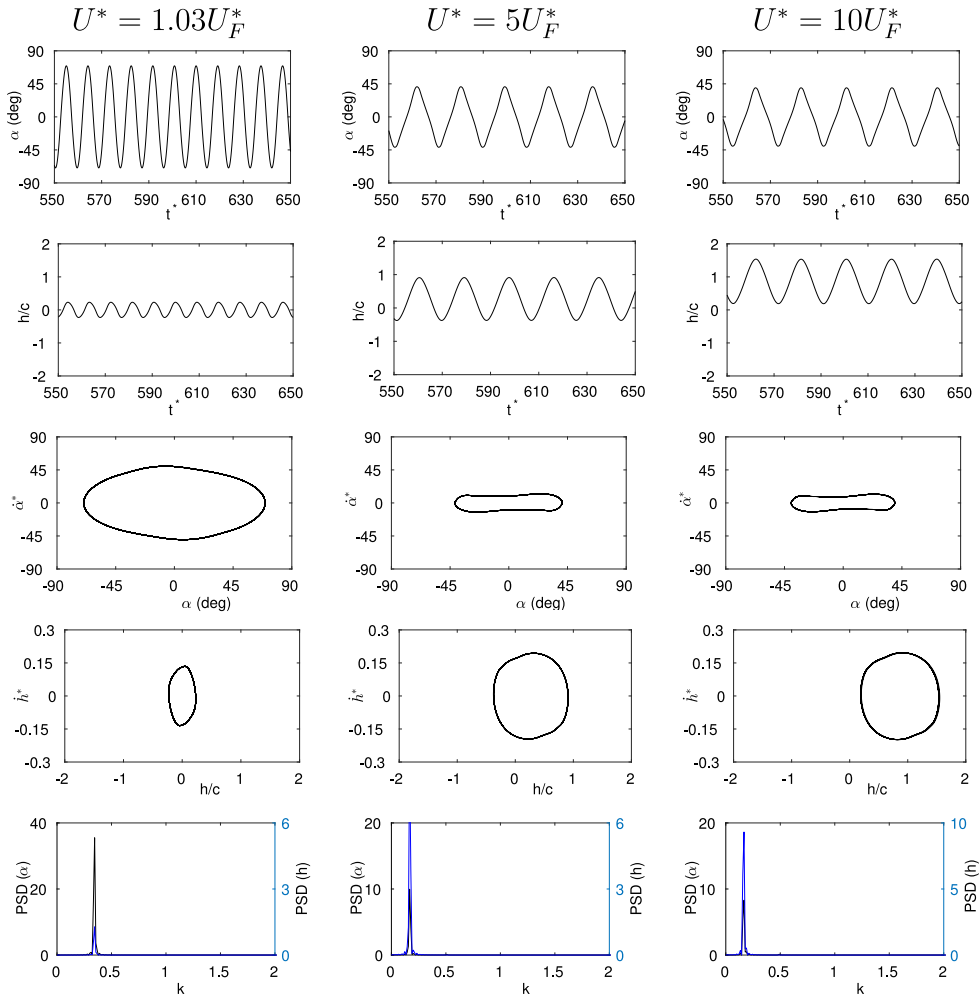
Fig. 7. Effect of freestream velocity: comparison of LCO characteristics for increasing values of U^* (from left to right). First row: pitch angle; second row: plunge per unit chord; third row: phase-plane plots for pitch; fourth row: phase-plane plots for plunge; fifth row: PSD plots (in dB/Hz) for pitch (left axis) and plunge (right axis).

three cases is presented in Fig. 7. The first and second rows in Fig. 7 show the oscillation response of the system in pitch and plunge respectively, after a "steady" (repeating) behavior is attained. Initially, as freestream velocity increases, the pitch response decreases in amplitude and becomes non-sinusoidal (though still periodic) while the plunge response increases in amplitude and also attains a nonzero mean value (drift). When the freestream velocity is increased even higher (from $5U_F^*$ to $10U_F^*$), the pitch response is unaffected while the main change in plunge response is the increase in mean drift.

The third and fourth rows in Fig. 7 show the phase-plane plots for pitch and plunge responses at the three freestream velocities. These confirm the earlier findings. The pitch response has a zero mean value at all velocities; as freestream velocity increases, the response first decreases in amplitude and becomes non-sinusoidal, and is subsequently unaffected. The plunge response starts off with a zero mean value which then increases with increasing velocity.

The fifth row of Fig. 7 contains the PSD plots for pitch and plunge oscillations. The reduced frequency of response decreases with increasing freestream velocity as is the same value for both pitch and plunge responses at all velocities.

The responses are stable and periodic even at high reduced frequencies, in contrast to the observations of Ramesh et al. (2015) that the LCOs become "multi-amplitude" and then divergent at high velocities. This is owing to the fact that the latter study was carried out in the limit of infinite Reynolds number whereas the present study is at $Re = 10{,}000$ where viscous effects dominate and provide stability to the system.

Vorticity contours for the three cases with different freestream velocities are shown in Fig. 8. Though the unsteady flows in all three cases are massively separated with large-scale flow separation and vortex shedding, the vortex structures for the lowest velocity are seen to be stronger and more concentrated. At high freestream velocities, the leading edge vortices formed are deformed and diffused/smeared before being shed into the wake. This is also a reflection of the reduced frequency decreasing with increasing freestream velocity. It is a well known result in unsteady fluid dynamics that high-k kinematics

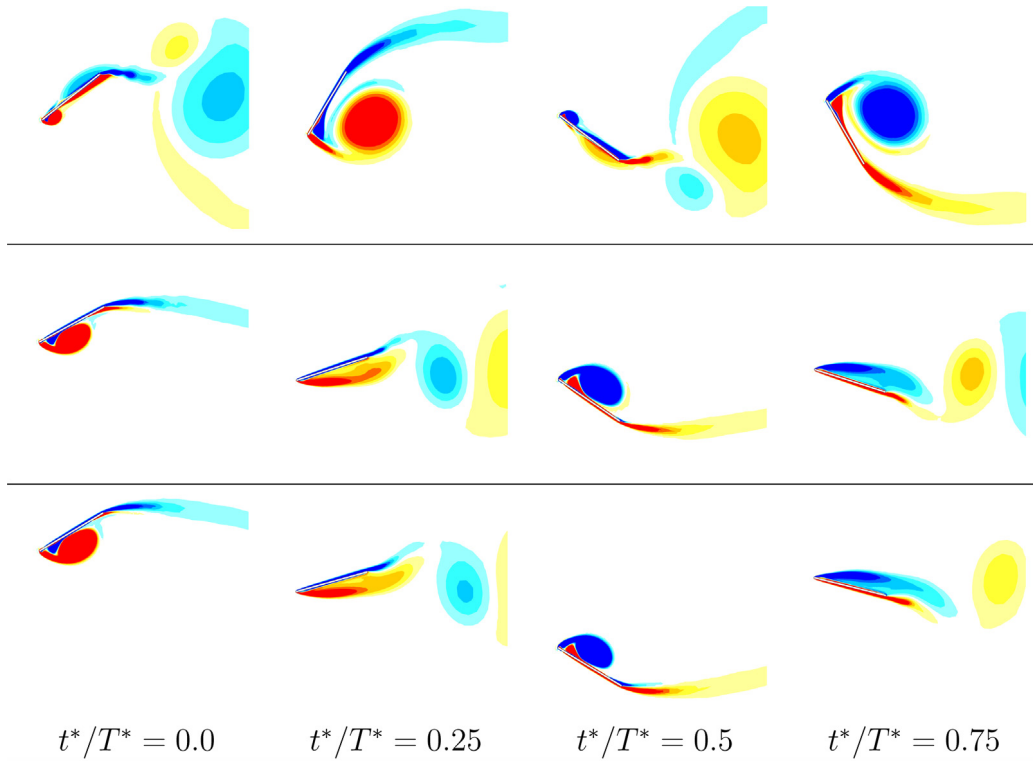$t^*/T^* = 0.0$ 　　　$t^*/T^* = 0.25$ 　　　$t^*/T^* = 0.5$ 　　　$t^*/T^* = 0.75$

Fig. 8. Effect of freestream velocity: comparison of vorticity contours at equally spaced instants during the response cycle. First row: $U^*/U_F^* = 1.03$; second row: $U^*/U_F^* = 5.0$, and third row: $U^*/U_F^* = 10.0$.
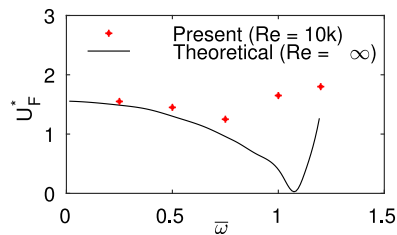

Fig. 9. Effect of frequency ratio: flutter velocity variation with frequency ratio ($\overline{\omega}$) compared against inviscid prediction from Murua et al. (2010).

lead to flows dominated by alternating and intermittent LEV shedding with negligible flow separation (akin to those seen in insect flight) while low-k kinematics lead to a dynamic-stall type behavior where the flow separation and LEV formation are coupled and the LEV is stretched before being shed into the wake (Ramesh et al., 2015).

3.3. Effect of frequency ratio

The effect of varying the frequency ratio which is a measure of the relative spring stiffnesses in plunge and pitch, is studied in this section. In addition to the baseline $\overline{\omega} = 0.25$, four additional values of 0.5, 0.75, 1.0 and 1.2 are considered. All other parameters are maintained at their baseline values. The onset of flutter depends strongly on this parameter, and the flutter velocities for the frequency ratios considered are shown in Fig. 9. The figure also shows the theoretical values of the flutter velocity for the same parameters from the theory of Theodorsen and Garrick (1942), published by Murua et al. (2010). We note that this latter flutter condition is determined in the inviscid limit of infinite Reynolds number.

In general, we observe that the flutter velocity at $Re = 10{,}000$ (present) is higher than the theoretical prediction, owing to the effects of viscosity and diffusion which increase the stability of the system. For $\overline{\omega} = 0.25$–0.75, the viscous flutter velocity is only slightly higher than the inviscid value. However, at frequency ratios of 1.0 and 1.2, large differences in the flutter velocity predictions are observed. The theoretical prediction (in the limit of infinite Reynolds number) shows a steep fall in the flutter velocity near $\overline{\omega} = 1$, which is not seen in the results from viscous simulations.
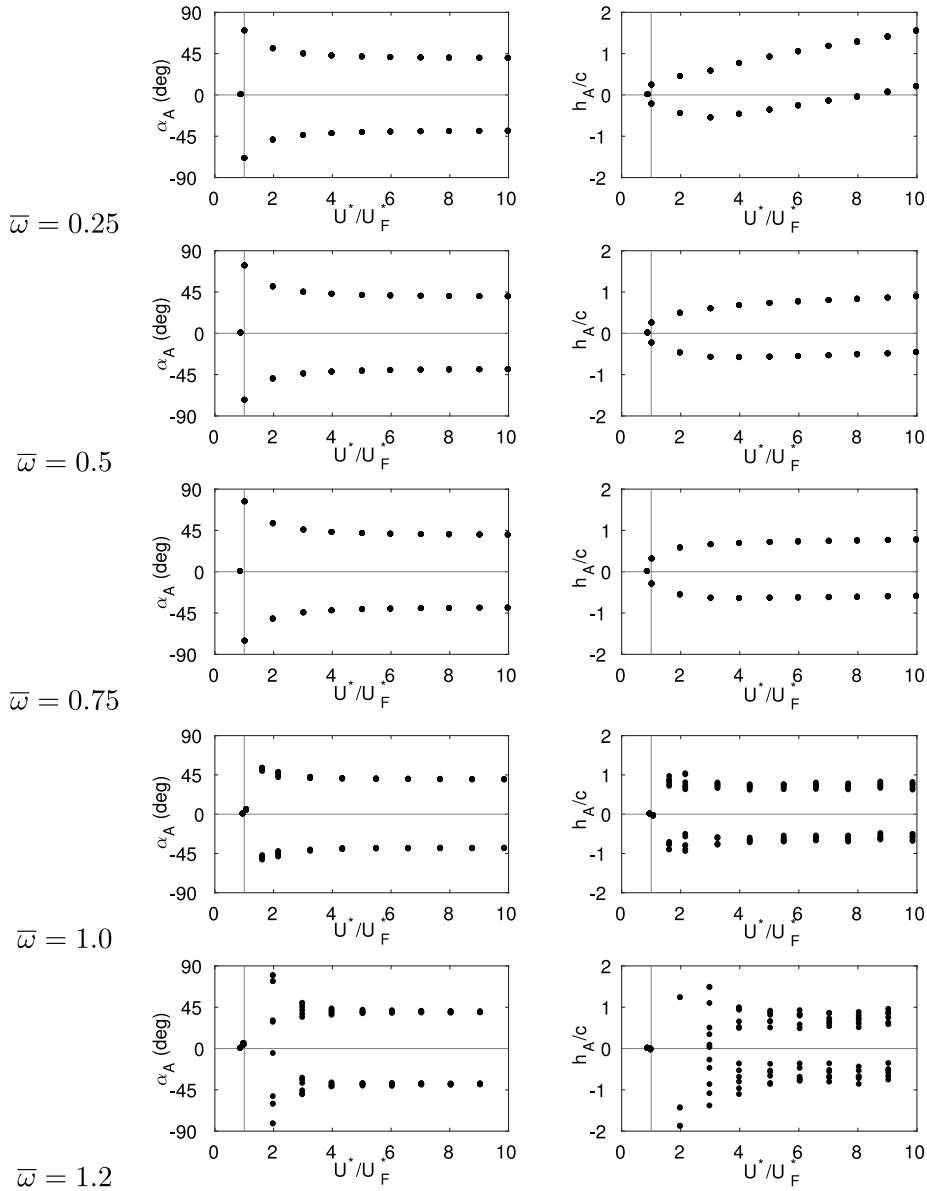
Fig. 10. Effect of frequency ratio: bifurcation characteristics of pitch (left) and plunge (right) with freestream velocity for different $\overline{\omega}$. The horizontal and vertical gray lines in the plots denote zero oscillation amplitude and $U^*/U_F^* = 1.0$ respectively.

In energy-harvesting systems that extract power from supercritical LCOs, the flutter velocity is also the "cut-in" speed for power generation. The lowest cut-in speed for this choice of parameters (Section 3.1) is seen to occur at $\overline{\omega} = 0.75$.

Fig. 10 shows bifurcation plots of pitch and plunge response against freestream velocity, for the different values of $\overline{\omega}$ discussed above. The data points for each value of freestream velocity in these plots are the pitch angle (α) when pitch rate is zero ($\dot{\alpha}^* = 0$), and the plunge displacement (h/c) when plunge rate is zero ($\dot{h}^* = 0$), respectively.

In the baseline case $\overline{\omega} = 0.25$, the pitch response is single-period with a mean value of zero for the full range of freestream velocity. The pitch amplitudes are highest at velocities just above the flutter velocity, and then reduce and become nearly constant after $U^*/U_F^* = 3$. The plunge responses are also single-period for the full range of velocities, but have a non-zero mean value (drift) after about $U^*/U_F^* = 3$. This drift increases with increasing freestream velocity.

As the frequency ratio is increased from $\overline{\omega} = 0.25$ to $\overline{\omega} = 0.75$, the stiffness of the translational spring is increased and consequently the drift in plunge response is seen to reduce (Fig. 10). At frequency ratio of $\overline{\omega} = 1$, the single-period behavior of the system is lost and both pitch and plunge responses evince oscillations with multiple amplitudes. An analysis of the response's power spectral density (in Section 3.4) shows that the response is not chaotic as there is no spread of frequencies. There is one dominant frequency peak similar to that seen in the earlier limit cycle oscillations (Figs. 5, 7), and in addition,
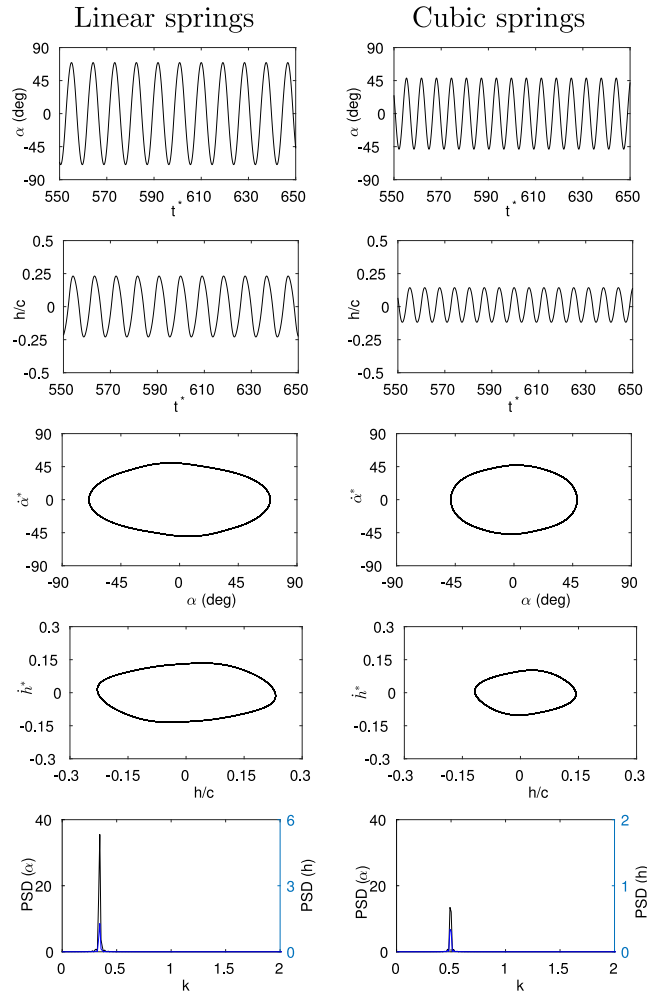
Fig. 11. Effect of cubic stiffening: comparison of LCO characteristics between linear springs ($\beta_\alpha = \beta_h = 0$) and cubic springs ($\beta_\alpha = \beta_h = 3$) at $\overline{\omega} = 0.25$ and $U^*/U_F^* = 1.03$. First row: pitch angle; second row: plunge displacement; third row: phase-plane plots for pitch; fourth row: phase-plane plots for plunge; fifth row: PSD plots (in dB/Hz) for pitch (left axis) and plunge (right axis).

there is a secondary frequency close in magnitude to the dominant one but with lower density. As a result of this secondary frequency, the system response changes from limit-cycle oscillations to "quasiperiodic" oscillations and the local maxima in these latter oscillations are no longer constant. These type of quasiperiodic oscillations in fluid–structure interaction have been reported by Ramesh et al. (2015), Sarkar and Bijl (2008) and Bose and Sarkar (2016). A detailed dynamical analysis of this phenomenon is beyond the scope of this paper. It is apparent that these oscillations with peaks of varying magnitudes are not suitable for the purpose of harvesting power. The frequency ratio of $\overline{\omega} = 1.2$ also exhibits oscillations with varying peaks at all values of freestream velocity above the flutter velocity.

3.4. Effect of cubic stiffening

In this section, the effect of positive cubic stiffening ("hard spring") on LCO characteristics in various regimes is studied.

In the first instance, the baseline parameters in Table 2 are considered but with $\beta_\alpha = \beta_h = 3$. The limit-cycle responses for $U^*/U_F^* = 1.03$ with linear and hard springs are compared in Fig. 11. Positive cubic stiffening in this case results in reduction of oscillation amplitude in both pitch and plunge. The phase-plane plots show that the addition of cubic stiffness makes the responses more harmonic in nature. The change in stiffness also affects the reduced frequency of the response, and both pitch and plunge responses are seen to have a higher reduced frequency than in the baseline case.

Next, the same cubic stiffening ($\beta_\alpha = \beta_h = 3$) is added to the baseline case at a higher freestream velocity, where $U^*/U_F^* = 5.0$. The plunge response with and without cubic stiffening is analyzed in Fig. 12. At this velocity, the system with linear springs shows a significant drift in plunge, i.e. a non-zero mean value. The addition of cubic stiffening results in a reduction in drift. This result is also illustrated through the phase-plane plots in Fig. 12.
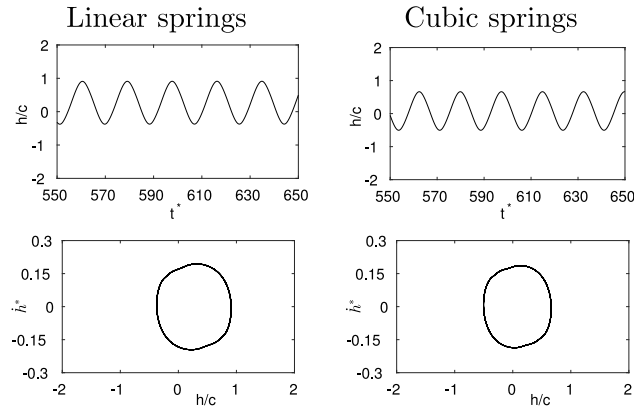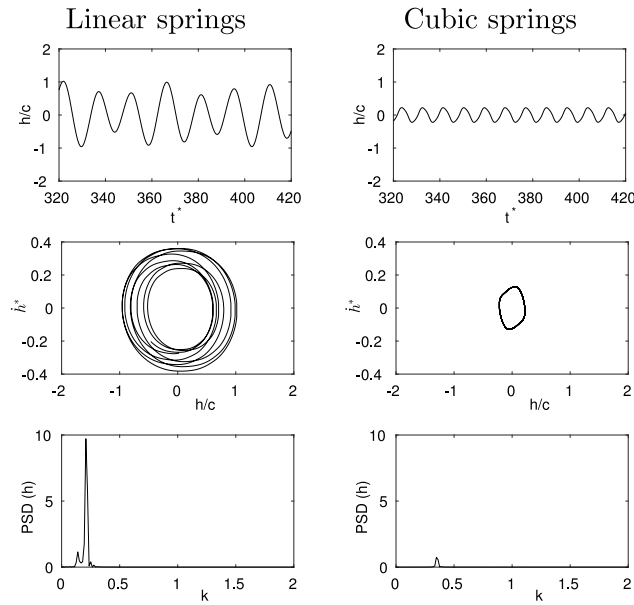
Fig. 12. Effect of cubic stiffening: comparison of LCO characteristics between linear springs ($\beta_\alpha = \beta_h = 0$) and cubic springs ($\beta_\alpha = \beta_h = 3$) at $\overline{\omega} = 0.25$ and $U^*/U_F^* = 5.0$. First row: plunge displacement; second row: phase-plane plots for plunge.

Fig. 13. Effect of cubic stiffening: comparison of LCO characteristics between linear springs ($\beta_\alpha = \beta_h = 0$) and cubic springs ($\beta_\alpha = \beta_h = 3$) at $\overline{\omega} = 1.0$ and $U^*/U_F^* = 2.0$. First row: plunge displacement; second row: phase-plane plots for plunge; third row: PSD plots (in dB/Hz) for plunge.

Finally, the aeroelastic system with frequency ratio $\overline{\omega} = 1.0$ is considered, at freestream velocity $U^*/U_F^* = 2.0$. The plunge response characteristics with linear and cubic springs are plotted in Fig. 13. As in the other two cases examined above, cubic stiffening is seen to impart stability to the aeroelastic system. The plunge displacement and phase-plane plots show that the quasiperiodic oscillations with the linear springs become single-period LCOs on addition of cubic stiffening. The PSD plot shows that the small secondary frequency disappears and that there is only fundamental frequency at a higher value than the baseline response frequency.

3.5. Effect of initial conditions

For a linear aeroelastic system, it is well known that only a supercritical bifurcation in response occurs at the flutter velocity (Lee et al., 1999b; Ramesh et al., 2015). For a system with nonlinearities however, a subcritical bifurcation is also possible which may result in limit-cycle oscillations at flow velocities below the flutter velocity. For the small baseline initial conditions considered in this research ($\alpha_0 = 10°$), no subcritical LCOs were observed. To investigate the influence of initial conditions, the baseline parameters with $U^*/U_F^* = 0.94$ (below flutter velocity) were considered along with two initial conditions: $\alpha_0 = 10°$ (small) and $\dot{\alpha}_0 = 60°/s$ (large). The comparison of responses is given in Fig. 14. For the small initial condition, the response converges to zero as already seen. For the large initial condition, the response of the aeroelastic
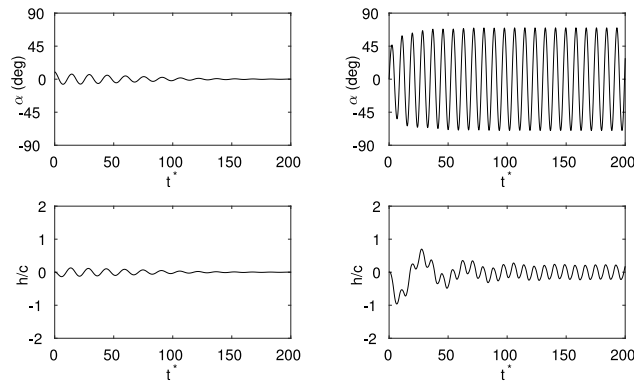
Fig. 14. Effect of initial conditions: response at $U^*/U_F^* = 0.94$ with other parameters at baseline value. Left: small initial condition of $\alpha_0 = 10°$, right: large initial condition of $\dot{\alpha}_0 = 60°/s$. Top row shows pitch angle and bottom row shows plunge displacement.

system develops into limit-cycle oscillations. Though the baseline structural dynamics is completely linear, the aerodynamic solution in this research is from the Navier–Stokes equations and may contain nonlinearities such as trailing-edge flow separation, resulting in LCOs. Such subcritical LCOs in an aeroelastic system have also been reported by Sarkar and Bijl (2008), for example.

3.6. Effect of power extraction (modeled through damping)

In the previous sections, we have studied the LCOs and dynamics of a perfectly elastic system without structural damping. In this section, we study the extraction of power from the system, modeled by viscous damping in plunge. First, the baseline case analyzed in Section 3.1 is considered with different values of damping ratio in plunge (0.1, 0.15, 0.2). The LCO properties for these cases are presented in Fig. 15. For the smaller two values of damping ratios, the LCO dynamics are not significantly affected and are similar to those of the baseline case. In the case of $\zeta_h = 0.2$ we see changes in plunge history and phase plane plots. Power extracted from the system increases proportionally with the damping factor as seen in the fourth row of Fig. 15. However, large values of damping ratio also modify the dynamics of the system, including the flutter onset velocity. For values of $\zeta_h > 0.2$ with the same freestream velocity, converged responses and no LCOs were observed.

In Section 3.2, LCOs were studied for flow velocities varying from U_F to $10U_F$. In Fig. 16, a similar study on the effect of velocity is conducted with damping $\zeta_h = 0.2$. The maximum power coefficient is obtained at a velocity just over the flutter velocity and drops rapidly for higher velocities.

The maximum power capture efficiency observed in this study is 4.4%. Researchers such as Kinsey and Dumas (2008) have reported efficiencies as high as 34% in an oscillating-foil system. In these cases however, a passive aeroelastic system was not considered; instead, an "ideal" combination of pitch and plunge kinematics corresponding to high power extraction efficiency were prescribed. It is unclear if these ideal kinematics can be obtained by a passive system through a suitable choice of parameters. This problem must be considered in future research.

4. Conclusions

Numerical aeroelastic simulations were performed to investigate limit-cycle oscillations of a 2DOF fully-passive flat plate at $Re = 10,000$. The effect of various system parameters on the onset of aerodynamic flutter and on the resulting system response characteristics were investigated.

The nondimensional flutter velocities determined in this research were different from the theoretical/inviscid values derived in the limit of infinite Re. The differences were especially pronounced for values of frequency ratios greater than 0.5. The flutter velocities in this research were always higher than the corresponding inviscid values, consistent with a more stable and viscous regime. For all frequency ratios considered, when the system was provided with small initial conditions, the response of the flat plate converged to zero if the freestream velocity was lower than the flutter velocity. At velocities greater than the flutter velocity, growing oscillations are seen, which are limited by nonlinearities such as fluid dynamic flow separation and vortex shedding, ultimately resulting in limit-cycle oscillations (supercritical). Subcritical limit-cycle oscillations at freestream velocities lower than the flutter velocity were observed when the system was provided with a large initial perturbation.

The aeroelastic system with frequency ratios between 0.25–0.75 evinced single-period LCOs for values of freestream velocity up to 10 times that of the corresponding flutter velocity. At velocities just over the flutter velocities, sinusoidal LCOs with high pitch amplitudes, low plunge amplitudes, high reduced frequencies and zero drift (mean value) in plunge were seen. With increase in freestream velocity, the responses became less sinusoidal, along with decrease in pitch amplitude, increase in plunge amplitude, decrease in reduced frequency and increase in plunge drift. At low values of freestream
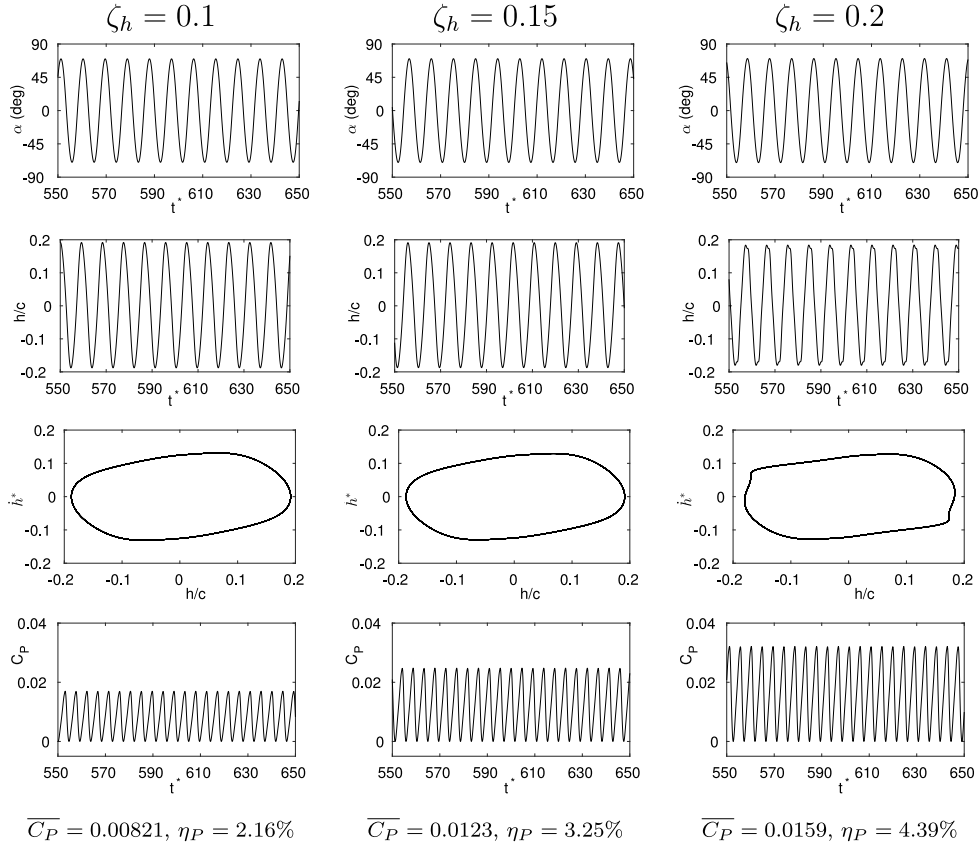
Fig. 15. Effect of damping ratio: comparison of LCO characteristics for increasing values of ζ_h (from left to right). First row: pitch angle; second row: plunge per unit chord; third row: phase-plane plots for plunge; fourth row: power coefficient.
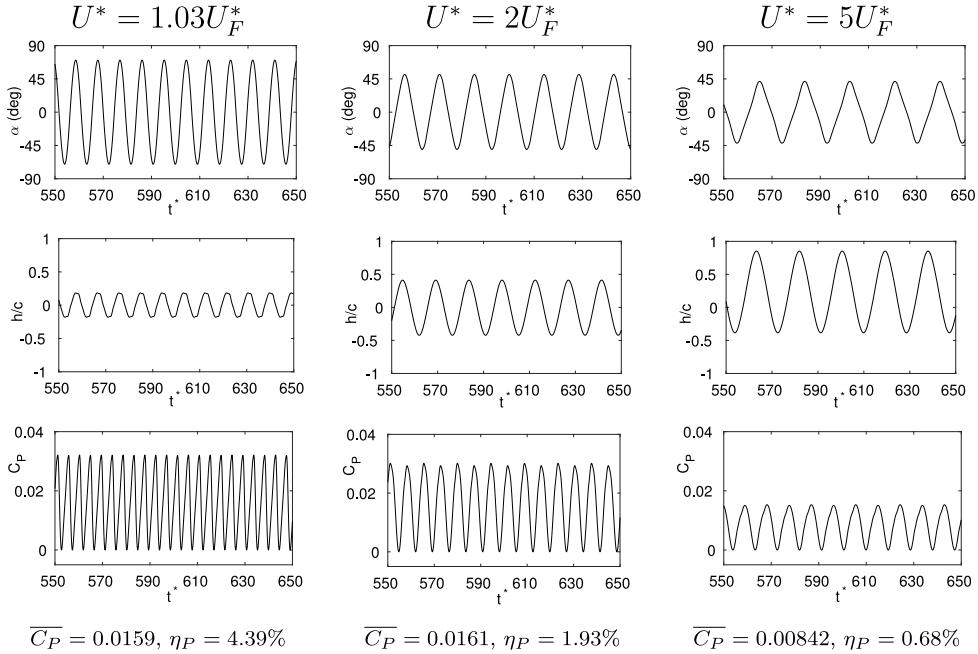

Fig. 16. Effect of freestream velocity (with damping): comparison of LCO characteristics for increasing values of ζ_h (from left to right). First row: pitch angle; second row: plunge per unit chord; third row: power coefficient.

velocity, the shed LEVs were stronger and more concentrated, while at higher velocities, they were more diffused/smeared. At frequency ratios of 1.0 and 1.2, the response had oscillations of varying peaks with a secondary frequency very close to the dominant one (quasiperiodic oscillations).

Cubic stiffening was seen to be a potentially beneficial addition to the aeroelastic system from the perspective of power harvesting. Positive cubic stiffening resulted in LCOs having reduced pitch and plunge amplitudes (corresponding to higher power extraction efficiencies) and higher frequencies. It also made the responses more sinusoidal and reduced the mean drift in plunge. The addition of cubic stiffening to the system was able to modify quasiperiodic oscillations (at high frequency ratios) into single-period oscillations.

Power extraction from the system was studied by introducing a viscous damping term in plunge to model the effect of the generator. The power coefficient was maximum at velocities just over the flutter velocity, and dropped in value for higher velocities. The power coefficient was seen to increase proportional to the value of damping ratio, though high values of the latter resulted in increase of flutter onset velocity. Notably, the power extraction efficiencies ($<5\%$) were smaller than those seen in other renewable energy technologies and in previous investigations of flapping-foil harvesters using prescribed kinematics. It is conceivable that higher efficiencies are possible with combinations of parameters other than those considered in this research (and at higher Reynolds numbers). The parameters here were chosen with a aim towards broadly identifying and classifying the dynamics of the aeroelastic system and not towards optimizing power extraction. Nevertheless, the "cut-in" flow velocities here are potentially lower than those required for competing technologies, with the highest power being available at velocities just slightly higher than the cut-in velocity. This makes the oscillating-foil harvester suitable for "scavenging" energy in low-speed flows such as in canals.

A good understanding of the basic aeroelastic system's dynamics at $Re = 10{,}000$ has been obtained through this research. More research is necessary to study in detail the influence of cubic stiffening and damping, and the properties of the system at higher Reynolds numbers. An optimization problem for maximizing power extraction through this system must also be undertaken. To investigate the system characteristics at higher Reynolds numbers, experimental/computational campaigns such as those performed in this research are recommended. For power optimization problems, the development of suitably validated low-order models (e.g. semi-empirical methods, discrete-vortex methods) is necessary owing to sheer expanse of the overall parameter space. These low-order models must be able to account for aerodynamic nonlinearities such as flow separation off the surface of the airfoil and leading-edge vortex shedding. They must also model viscous diffusion in order to predict the correct flutter velocity at low Reynolds numbers. The qualitative and quantitative results obtained through this research provide a good basis for the development and validation of such low-order models.

Acknowledgments

References

Amandolese, S., Michelin, X., Choquel, M., 2013. Low speed flutter and limit cycle oscillations of two-degree-of-freedom flat plate in a wind tunnel. J. Fluids Struct. 43, 244–255.

Anderson, J., Streitlien, K., Barrett, D., Triantafyllou, M., 1998. Oscillating foils of high propulsive efficiency. J. Fluid Mech. 360 (1), 41–72.

Bendiksen, O.O., 2011. Review of unsteady transonic aerodynamics: Theory and applications. Prog. Aerosp. Sci. 47 (2), 135–167.

Bisplinghoff, R.L., Ashley, H., 1996. Aeroelasticity. Courier Dover Publications.

Boccalero, G., Olivieri, S., Mazzino, A., Boragno, C., 2017. Power harvesting by electromagnetic coupling from wind-induced limit cycle oscillations. Smart Mater. Struct. 26 (9), 095031.

Boragno, C., Festa, R., Mazzino, A., 2012. Elastically bounded flapping wing for energy harvesting. Appl. Phys. Lett. 100 (25), 253906.

Bose, C., Sarkar, S., 2016. Flexible Flapping Wings can Exhibit Quasi-periodic Motion! Vol. 759. IOP Publishing, pp. 1–7.

Bryant, M., Gomez, J.C., Garcia, E., 2013. Reduced-order aerodynamic modeling of flapping wing energy harvesting at low Reynolds number. AIAA J. 51 (12), 2771–2782.

Catalano, P., Tognaccini, R., 2010. Turbulence modeling for low-Reynolds-number flows. AIAA J. 48 (8), 1673–1685.

Dickinson, M.H., Gotz, K.G., 1993. Unsteady aerodynamic performance of model wings at low Reynolds numbers. J. Exp. Biol. 174 (1), 45–64.

Dunnmon, J.A., Stanton, S.C., Mann, B.P., Dowell, E.H., 2011. Power extraction from aeroelastic limit cycle oscillations. J. Fluids Struct. 27 (8), 1182–1198.

Ellington, C.P., 1999. The novel aerodynamics of insect flight: applications to micro-air vehicles. J. Exp. Biol. 202 (23), 3439–3448.

Ellington, C.P., van den Berg, C., Willmott, A.P., Thomas, A.L.R., 1996. Leading-edge vortices in insect flight. Nature 384 (1), 626–630.

Fung, Y., 2002. An Introduction to the Theory of Aeroelasticity. Courier Dover Publications.

Hamamoto, M., Ohta, Y., Hara, K., Hisada, T., 2007. Application of fluid–structure interaction analysis to flapping flight of insects with deformable wings. Adv. Robot. 21 (1–2), 1–21.

Hammer, P., Altman, A., Eastep, F., 2014. Validation of a discrete vortex method for low reynolds number unsteady flows. AIAA J. 52 (3), 643–649. http://dx.doi.org/10.2514/1.J052510.

Jones, K.D., Lindsey, K., Platzer, M.F., 2003. An investigation of the fluid-structure interaction in an oscillating-wing micro-hydropower generator. Trans. Built Environ. 71.

Jones, K., Platzer, M., Jones, K., Platzer, M., 0000. Numerical computation of flapping-wing propulsion and power extraction, AIAA Paper 1997–0826.

Kamakoti, R., Shyy, W., 2004. Fluid–structure interaction for aeroelastic applications. Prog. Aerosp. Sci. 40 (8), 535–558.

Kinsey, T., Dumas, G., 2008. Parametric study of an oscillating airfoil in a power-extraction regime. AIAA J. 46 (6), 1318–1330.

Lee, B.H.K., Jiang, L.Y., Wong, Y.S., 1999a. Flutter of an airfoil with a cubic restoring force. J. Fluids Struct. 13 (1), 75–101.

Lee, B.H.K., Price, S.J., Wong, Y.S., 1999b. Nonlinear aeroelastic analysis of airfoils: bifurcation and chaos. Prog. Aerosp. Sci. 35 (3), 205–334.

Leishman, J.G., 2002. Principles of Helicopter Aerodynamics. Cambridge Aerospace Series.

Liu, Z., Lai, J.C.S., Young, J., Tian, F., 2016. Discrete vortex method with flow separation corrections for flapping-foil power generators. AIAA J..

McGowan, G.Z., Granlund, K., Ol, M.V., Gopalarathnam, A., Edwards, J.R., 2011. Investigations of lift-based pitch-plunge equivalence for airfoils at low Reynolds numbers. AIAA J. 49 (7), 1511–1524.

McKinney, W., DeLaurier, J., 1981. Wingmill: an oscillating-wing windmill. J. Energy 5 (2), 109–115.

Murua, J., Palacios, R., Peiró, J., 2010. Camber effects in the dynamic aeroelasticity of compliant airfoils. J. Fluids Struct. 26 (4), 527–543.

Nakata, T., Liu, H., 2012. Aerodynamic performance of a hovering hawkmoth with flexible wings: a computational approach. Proc. Roy. Soc. B Biol. Sci. 279 (1729), 722–731.

Newmark, N.M., 1959. A method of computation for structural dynamics. J. Eng. Mech. Div. 85 (EM3), 67–94.

Ol, M.V., Altman, A., Eldredge, J.D., Garmann, D., Lian, Y., 2010. Résumé of the AIAA FDTC low Reynolds number discussion groups canonical cases, AIAA paper 2010–1085.

Ol, M.V., Bernal, L., Kang, C.K., Shyy, W., 2009. Shallow and deep dynamic stall for flapping low Reynolds number airfoils. Exp. Fluids 46 (5), 883–901.

Peng, Z., Zhu, Q., 2009. Energy harvesting through flow-induced oscillations of a foil. Phys. Fluids 21 (123602).

Price, S.J., Alighanbari, H., Lee, B.H.K., 1995. The aeroelastic response of a two-dimensional airfoil with bilinear and cubic structural nonlinearities. J. Fluids Struct. 9 (2), 175–193.

Ramesh, K., Gopalarathnam, A., Edwards, J.R., Ol, M.V., Granlund, K., 2013. An unsteady airfoil theory applied to pitching motions validated against experiment and computation. Theor. Comput. Fluid Dyn. 27 (6), 843–864.

Ramesh, K., Gopalarathnam, A., Granlund, K., Ol, M.V., Edwards, J.R., 2014. Discrete-vortex method with novel shedding criterion for unsteady airfoil flows with intermittent leading-edge vortex shedding. J. Fluid Mech. 751, 500–538.

Ramesh, K., Murua, J., Gopalarathnam, A., 2015. Limit-cycle oscillations in unsteady flows dominated by intermittent leading-edge vortex shedding. J. Fluids Struct. 55, 84–105.

Roache, P.J., 1998. Verification of codes and calculations. AIAA J. 36 (5), 696–702.

Sarkar, S., Bijl, H., 2008. Nonlinear aeroelastic behavior of an oscillating airfoil during stall-induced vibration. J. Fluids Struct. 24 (6), 757–777.

Shimizu, E., Isogai, K., Obayashi, S., 2008. Multiobjective design study of a flapping wing power generator. J. Fluids Eng. 130 (2), 021104.

Shyy, W., Liu, H., 2007. Flapping wings and aerodynamic lift: The role of leading-edge vortices. AIAA J. 45 (12).

Spalart, P.R., Allmaras, S.R., 1992. A one-equation turbulence model for aerodynamic flows, AIAA Paper 92–0439.

Taylor, G.K., Triantafyllou, M.S., Tropea, C., 2010. Animal Locomotion. Springer-Verlag.

Theodorsen, T., 1935. General theory of aerodynamic instability and the mechanism of flutter, NACA Rept. 496.

Theodorsen, T., Garrick, I.E., 1942. Flutter calculations in three degrees of freedom, NACA Rept. 741.

Travin, A., Shur, M., Strelets, M., Spalart, P., 2000. Detached-eddy simulations past a circular cylinder. Flow Turbul. Combust. 63, 293–313.

Viola, I., Bot, P., Riotte, M., 2013. On the uncertainty of cfd in sail aerodynamics. Internat. J. Numer. Methods Fluids 72 (11), 1146–1164.

Visbal, M.R., 2009. High-fidelity simulation of transitional flows past a plunging airfoil. AIAA J. 47 (11), 2685–2697.

Wang, Z., Du, L., Zhao, J., Sun, X., 2017. Structural response and energy extraction from a fully passive flapping foil. J. Fluids Struct. 72, 96–113.

Wang, C., Eldredge, J.D., 2012. Low-order phenomenological modeling of leading-edge vortex formation. Theor. Comput. Fluid Dyn. 27 (5), 577–598.

Xia, X., Mohseni, K., 2013. Lift evaluation of a two-dimensional pitching flat plate. Phys. Fluids 25 (9), http://dx.doi.org/10.1063/1.4819878, URL http://scitation.aip.org/content/aip/journal/pof2/25/9/10.1063/1.4819878.

Xiao, Q., Zhu, Q., 2014. A review on flow energy harvesters based on flapping foils. J. Fluids Struct. 46, 174–191.

Young, J., Ashraf, M.A., Lai, J.C.S., Platzer, M.F., 2013. Numerical simulation of fully passive flapping foil power generation. AIAA J. 51 (11), 2727–2739.

Young, J., Lai, J., Platzer, M.F., 2014. A review of progress and challenges in flapping foil power generation. Prog. Aerosp. Sci. 67, 2–28.

Zhu, Q., Haase, M., Wu, C.H., 2009. Modeling the capacity of a novel flow-energy harvester. Appl. Math. Model. 33 (5), 2207–2217.

Zhu, Q., Peng, Z., 2009. Mode coupling and flow energy harvesting by a flapping foil. Phys. Fluids 21 (3), 033601.